HypoQuantyl: a Machine Learning-based Tool for the Kinematic Analysis of Hypocotyl Growth Demonstrated on Arabidopsis *cry1*, *phot1*, and *phyB* Photoreceptor Mutants

by

Julian A. Bustamante

A dissertation submitted in partial fulfillment of

the requirements for the degree of

Doctor of Philosophy

(Cellular and Molecular Biology)

at the

University of Wisconsin - Madison

2023

Date of final oral examination: 12/13/2023

This dissertation is approved by the following members of the Final Oral Committee:

Edgar Spalding, Professor, Botany
Jean-Michel Ané, Professor, Bacteriology
Richard Amasino, Professor, Botany
Simon Gilroy, Professor, Botany
Yu Hen Hu, Professor, Electrical and Computer Engineering

Abstract

The hypocotyl (juvenile stem) of an *Arabidopsis thaliana* seedling elongates quickly in darkness. Light acting through photoreceptors in the cryptochrome, phototropin, and phytochrome families inhibit this extension as part of the photomorphogenic development of the seedling. Previous studies characterized the timing but not the location along the hypocotyl of the growth inhibition induced by light. Here we describe custom software called HypoQuantyl that can determine where growth occurs along the hypocotyl and where light inhibits it by analyzing time series of digital images. HypoQuantyl is an algorithm that integrates ground truth data, and anatomically relevant anchor points to predict the contour of the hypocotyl. The contour is used to determine a midline, and the midline is used to refine the contour. In a recursive fashion, HypoQuantyl ultimately produces a midline that traces the hypocotyl and terminates at the cotyledonary node. Then, optical flow techniques and kinematic concepts are used to analyze times lapse image data to map relative elemental growth rates along the hypocotyl. Dark-grown hypocotyl material expanded at rates as high as 4% h^{-1} mostly between 0.4 and 1.5 mm below the cotyledon-hypocotyl junction. Blue light acting though the phototropin 1 photoreceptor (PHOT1) rapidly inhibited expansion in this growth zone. The cryptochrome 1 (CRY1) blue light receptor affected a different region of the hypocotyl. The long hypocotyl phenotype of a *cryptochrome 1* (*cry1*) mutant begins to develop 30 min after the onset of illumination when expansion within the most apical 0.1-0.3 mm of the hypocotyl accelerates to 6% h^{-1}. This novel region of rapid expansion in *cry1* lies above the regular growth zone. Red light-induced inhibition mediated by the phytochrome B (PhyB) photoreceptor occurs in the regular growth zone. The long hypocotyl phenotype of a *phyB* mutant in red light is due to weak

inhibition below 0.6 mm, not to activating a previously non-growing region as in *cry1*. Thus, the similar long-hypocotyl phenotypes of *cry1* and *phyB* in blue and red light, respectively, have profoundly different kinematic bases. These HypoQuantyl-derived results indicate when and where to focus future mechanistic studies of photoreceptor function.

Table of Contents

Table of Figures

Introduction

Plants rely on light as their primary energy source, which is probably why they use light as a source of information to guide their growth and development. Photomorphogenesis is a broad term that describes how plant growth and development is affected by light acting as information rather than energy. Photomorphogenesis requires photoreceptor proteins to detect and decode the light signals (Arsovski et al., 2012). Researchers have used light-induced inhibition of hypocotyl elongation, a component of seedling photomorphogenesis, as a model for elucidating the molecular mechanisms of photoreceptor action, primarily because mutations may produce long-hypocotyl phenotypes that are easy to score in genetic screens, and measuring hypocotyl length is straightforward when quantification is necessary. Indeed, Ahmad and Cashmore (1993) discovered the cryptochrome 1 (CRY1) blue-light receptor, the first of its kind in plants, by identifying the gene responsible for the long hypocotyl that *hy4* mutants (now called *cry1*) display when grown in continuous high-irradiance blue light for a few days (Figure 1). Hypocotyl length assays demonstrated that phytochrome B (PHYB) is the photoreceptor responsible for the inhibitory effect of long-term red light (Somers et al., 1991) and that PhyA is the photoreceptor responsible for the long-term effects of far-red light (Parks and Quail, 1993). While end-point hypocotyl lengths have provided critical information in innumerable studies of photoreceptor action, and

Figure 1. Long hypocotyl phenotype. A cry1 mutant seedling compared to the wild type, both grown in continuous blue light for 5 days.

continue to do so, end-point assays cannot provide temporal information about the affected process. Knowing when a mutant phenotype begins to develop is evidence of when the affected factor, typically a protein, begins to function in the process.

Electronic linear variable displacement transducers (LVDTs) can measure hypocotyl elongation continuously with high resolution (Meijer, 1968; Cosgrove, 1988; Spalding and Cosgrove, 1989), even in small Arabidopsis seedlings (Parks et al., 1998; Parks and Spalding, 1999). Transducer results showed that blue light strongly inhibits hypocotyl elongation after a lag time measured in seconds, while it takes several minutes for red light to initiate a slower, weaker inhibition (Meijer, 1968; Cosgrove, 1982).

Computational analysis of digital images acquired as a time series is another approach to measuring hypocotyl growth (Dowson-Day and Millar, 1999; Folta and Spalding, 2001). It has the potential to be high throughput, unlike transducer-based methods. Automated cameras and image processing can combine to measure growth rate accurately at intervals of five or ten minutes over several hours to provide a highly resolved time course of light responses, even in Arabidopsis seedlings that may be only 3 mm long at the beginning of an experiment (Miller et al., 2007; Wang et al., 2009). When used to compare mutants to the wild type, time course analyses can show when a photoreceptor begins to influence elongation, and for how long. For example, *phyA* does not display a long hypocotyl when grown in continuous red light for 3-5 days (Parks and Quail, 1993) but a time course analysis showed that PHYA initiates the response to red light and controls it for the first three hours. After that point, the PHYB receptor establishes and sustains the inhibition and the PHYA contribution wanes (Parks et al., 1998). Time course analysis of blue light-induced inhibition indicated that this exceptionally rapid

response is also a sequence of separate photoreceptor actions. The phototropin 1 (PHOT1) receptor controls the immediate-early phase of the inhibition (Folta and Spalding, 2001). An end-point hypocotyl length assay cannot detect this initial, apparently transient, component of the mechanism. Conversely, *cry1* responds with an initial phase of inhibition identical to the wild type (Parks et al., 1998; Folta and Spalding, 2001), because PHOT1 is the controlling photoreceptor. The long hypocotyl phenotype of *cry1* that becomes evident after hours or days of growth in blue light is the result of fast elongation that develops 30 min after illumination. Another study showed that the nuclear pool of CRY1, not the cytoplasmic pool, is responsible for the apparent long-term maintenance of this post-PHOT1 inhibition (Wu and Spalding, 2007). Apparently, PHOT1 at the plasma membrane (Sakamoto and Briggs, 2002) rapidly initiates a transient phase of growth inhibition, which nuclear CRY1 sustains after a lag time of 30 min. These time-course measurements of hypocotyl growth rate do not show which region of the hypocotyl is expanding, or which region does not respond in long-hypocotyl mutants such as *cry1*. Obtaining information about the spatial distribution of growth along the hypocotyl depends on the ability to track the displacement of many small material elements, and then interpreting their movements relative to each other using the concepts and methods of kinematics (Silk and Erickson, 1979). In larger species, applied marks such as ink dots can be tracked through image sequences to provide the raw data (Spalding and Cosgrove, 1993). The Arabidopsis inflorescence stem has been physically marked to map regions of greatest local extension after collecting images (Hall and Ellis, 2012). Arabidopsis hypocotyls are too small to mark effectively but endogenous brightness variation (texture) in grayscale digital images can serve as unique features to track. The authors of the KymoRod software (Bastien et al., 2016)

took this approach. KymoRod results demonstrated that the dark-grown (etiolated) Arabidopsis hypocotyl has a growth zone approximately 2 mm long located a short distance below the apical hook. To be useful in a study of light-induced hypocotyl growth inhibition, the method must be able to track material only within the hypocotyl and reference it to a position along the midline. It is generally not difficult to automatically isolate ('segment' is the term used in image analysis) the seedling from background in a high-contrast image and determine its midline, but it is difficult to determine where the midline should terminate to exclude the cotyledons (embryonic leaves), especially when the apical hook is so tightly closed that they contact the hypocotyl. The midline that KymoRod and the method of Miller et al. (2007) extracted from the segmented seedling included the cotyledons, so some manual pre- or post-processing steps were required to isolate only the hypocotyl. In studies of seedling photomorphogenesis, the growth and movement of the cotyledons limited the usefulness of methods that could not isolate the hypocotyl. Wang et al. (2009) devised a semi-automatic method for terminating the hypocotyl midline at the appropriate junction, the cotyledonary node, so that hypocotyl elongation could be tracked at 5 min intervals. HYPOTrace took advantage of a distinguishing feature detectable in suitably oriented seedlings. HYPOTrace required high-contrast images to function well, which minimized the texture a kinematics method would rely on to track material flow. Thus, to date, an image processing tool that can automatically segment specifically the hypocotyl and track patches of texture to determine the spatial distribution of material expansion as a seedling responds to light has not been produced. Therefore, lack of an appropriate tool has prevented a kinematic analysis of seedling hypocotyls responding to light. Consequently, spatial and temporal details of photoreceptor action during a critical phase of

plant growth and development remain unknown. Here we report the creation of a tool called HypoQuantyl that can automatically measure the spatial distribution of hypocotyl material expansion in terms of kinematics. The challenges of isolating the hypocotyl from the cotyledons and determining a midline that terminates at the appropriate location were solved by creating a custom machine learning-enabled pipeline. Patch tracking for kinematic analysis was achieved by incorporating a modified version of a recently published method (Henry et al., 2023). Results obtained with the HypoQuantyl pipeline can focus future cellular, molecular, and biochemical investigations on the right cells at the right time to determine how photoreceptors control hypocotyl cell expansion.

Results

HypoQuantyl is a custom software pipeline that automatically analyzes Arabidopsis hypocotyl elongation in kinematic terms. The kinematic analysis of hypocotyl growth requires tracking material elements as they move at many locations along the principal geometric feature of the organ, its midline (Aris, 2012; Erickson, 1980; Silk, 1979). The midline must include the tightly curved region called the apical hook, but not extend into the cotyledons or the petioles that attach them to the hypocotyl at the cotyledonary node. The midline can be determined from the hypocotyl's contour. Simple segmentation methods will not faithfully isolate a contour from which a hypocotyl midline can be determined because the cotyledonary node lacks any feature that a standard, contrast-based method can reliably distinguish to terminate the midline, and the cotyledons sometimes touch the flank of the hypocotyl, which would deflect a midline based on simple binary object morphology. Furthermore, the apical hook opens and the cotyledons spread into unpredictable shapes in response to the (light) treatment during the

experiment. HypoQuantyl is a machine-learning based solution to these challenges.

The raw data are time series of grayscale images of Arabidopsis seedlings growing in total darkness before receiving a light treatment (Figure 2). Ground truth data were required to train the convolutional neural networks that HypoQuantyl uses to find a hypocotyl-specific midline that orients the optical flow-based patch tracking that produces the kinematic analysis of growth. The ground truth data set was obtained by a combination of automatic image processing steps and manual labeling in the form of tracing and point selections. An example of an image to be analyzed is shown in Figure 2A, which also illustrates the first steps in the process of creating the ground truth data.

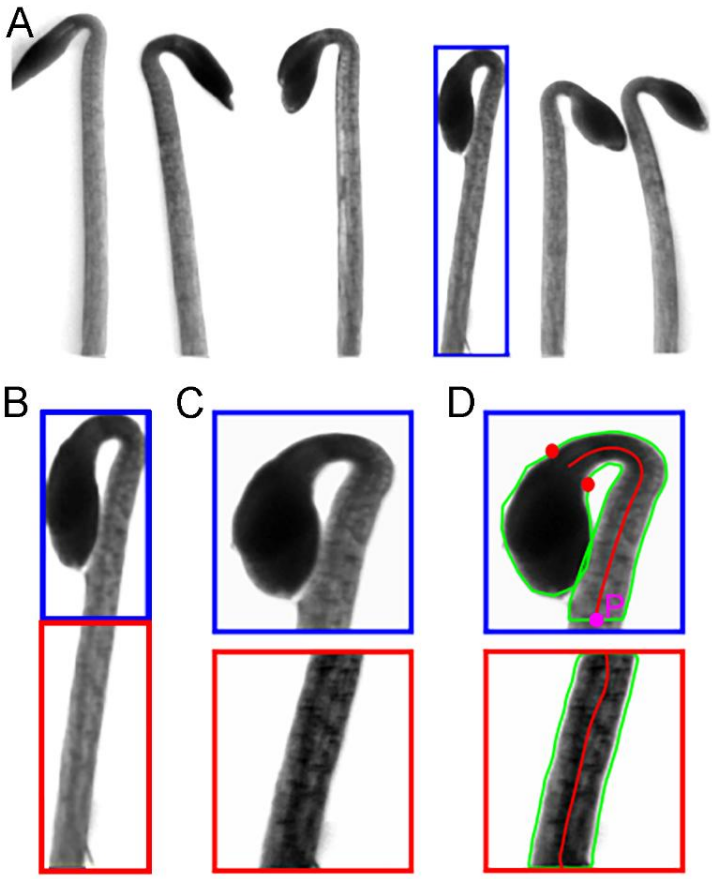

Figure 2. Example of the images to be analyzed and the first steps in the process of creating the ground truth data used to train the machine learning algorithms. A) An image containing six Arabidopsis seedlings from a time series. A blue box around one seedling shows how each seedling would be cropped from the image. B) The hypocotyl is divided into upper and lower sections because the upper section poses segmentation challenges that require a machine learning-based solution. C) Each section from every seedling is rescaled to be an equal 201 x 201 square. D) Ground truth contour (green), manually selected cotyledonary node points (red circles), and central base point P produce a ground truth midline (red line).

Creating the HypoQuantyl method

Simple contrast-based (thresholding) segmentation (Otsu, 1979) isolated each seedling in a

frame from background. A bounding box cropped each seedling into a rectangular image (Figure 1A). Each cropped image was divided at a point 250 pixels below the top to create upper and lower sub images (Figure 2B). This step was taken because the lower sub image contained an uncomplicated portion of the hypocotyl while the upper sub image presented the segmentation challenges that required a machine learning approach.

The upper and lower sub images were both re-scaled into 201 x 201 squares (Figure 2C). Upper sub images from a group of 550 seedlings representing different stages of the light experiment and thus a wide variety of shapes and segmentation challenges were selected to produce a ground truth segmentation data set. Some of these could be segmented automatically with a simple threshold method while many others required manual tracing of the contour. Figure 2D shows a manually traced contour (green line) and two points selected to clip the contour at the cotyledonary node (red circles). A single selection marked the center of the base of the hypocotyl (P). From these inputs, a ground truth midline was constructed (red line). Usually, the cotyledons were in profile, facing either left or right. The images were standardized to be left-facing by mirroring the coordinates of right-facing examples. These clipped and left-facing contours, divided into four sections, form the basis of the segmentation pipeline used to train our machine learning algorithms. The next step uses these ground-truth labeled images to produce a mathematical structure we call a Z vector (Z_V). It will form a scaffold for contour construction. Figure 3 illustrates the steps taken to create the components of Z_V. Figure 3A shows the contour, selected cotyledon node points, the base point P, and two cotyledon domains that contribute information. A portion of a complete contour defined by a window of size w (magenta line in Figure 3B) is selected. A point b (yellow circle) is the midpoint of a line

that connects the two ends of this segment. A tangent vector T and a normal vector N form a frame F at b. This point b and its reference frame form an element in Z_V. The window is slid along the contour to complete the Z_V scaffold (Figure 3C). Machine learning methods were implemented to train the HypoQuantyl algorithm to displace each point b as illustrated in Figure 3D to form an accurate contour vector C_V.

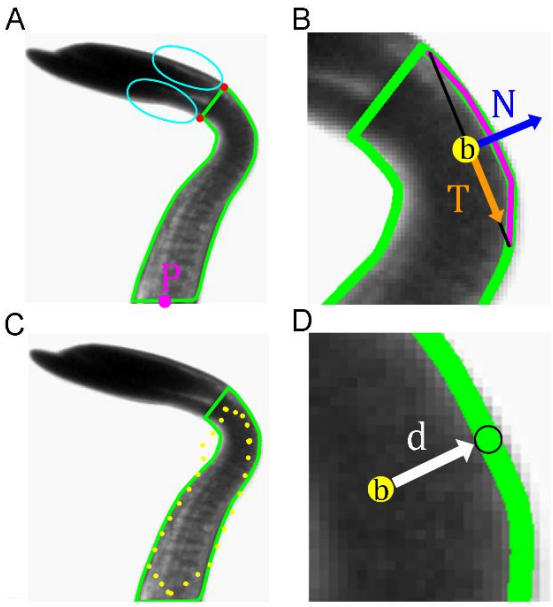

Figure 3. Steps preparatory to predicting the contour of a hypocotyl. A) Depiction of the ground truth marks: contour, base point, and two cotyledonary node selections that are used to position two domains for sampling the cotyledon side of the node. B) A segment of the contour (magenta line) and its midpoint b in a reference frame F formed by normal (N) and tangent (T) vectors. C) Sliding the window over the entire contour builds up a sequence of base points and their attached reference frames, which collectively comprise the Z_V. D) The HypoQuantyl algorithm is trained to predict a vector d that will displace b to its proper position on the contour.

Complex objects such as curves may be represented as vectors in low (L) or high (E) dimensional embeddings (Pearson, 1901). The high dimensional vector representation of a general object X is X_V and the low dimensional embedding is X_S. In the following description, X_V will correspond with the reshaping of the data in column-major order $(\mathrm{vec}(\mathrm{X}) \triangleq \mathrm{X}_v)$. The vector X_V results from projecting from a vector space of dimension L to a vector space of

dimension E using an affine transformation $\gamma_X \triangleq [F, U]$. In this description of the HypoQuantyl pipeline, F contains orthonormal column vectors ($F_{ij}F_{ik} = \delta_{ik}$) in a matrix of size $[E, L]$, and is derived from the eigenvector decomposition of the covariance matrix constructed from (a) number of samples of (X_v^a). The offset (U) of the frame F is the mean of the samples (X_v^a) and is an E dimensional vector. This, we may summarize a complex object X as $[\mathrm{K}, \mathrm{E}, \mathrm{L}, \gamma_x, \mathrm{PER}] \triangleq R_x$ where K is the size of the natural representation of X, E is the dimensionality of X_V, L is the dimensionality of X_S, γ_x maps X_S to X_V, and PER is the percent variance explained.

The HypoQuantyl pipeline relies on sampling pixel information at a location within a complex object and with respect to a reference frame F to either shift or grade (quantitatively score) a curve. In these cases, F is attached to a point b, i.e. $[F, b]$ (Cartan, 1925; Ehresmann, 1950). This construction moves a point *x* from the frame F at a position b into the origin's frame such that $x' = [F, b] \cdot x = F \cdot x + b$. We will simplify $[F, b]$ into a single construct E so that $x' = E \cdot x$. The structure E can be extended from a point b to a sequence of points which constitute a curve B and the corresponding construct $[F, B]$. The total space E then consists of two parts, an underlying base structure B and a frame structure F, which are rotated and translated copies of F placed at each site on B. The total space E serves to map a location *x* on the base structure to a location in the image. Sampling the image at *x* in the total space E amounts to mapping the position from within the total space $(E \cdot x)$ to the image frame and sampling the image as $I(E \cdot x)$.

This explanation of the concepts that the symbols represent, and the constructions will aid the description of the machine learning-enabled midline discovery portion of the HypoQuantyl kinematics pipeline. This portion consists of the S-phase, the C-cycle, and the R-cycle. Figure 4 and the text are meant to mutually support each other.

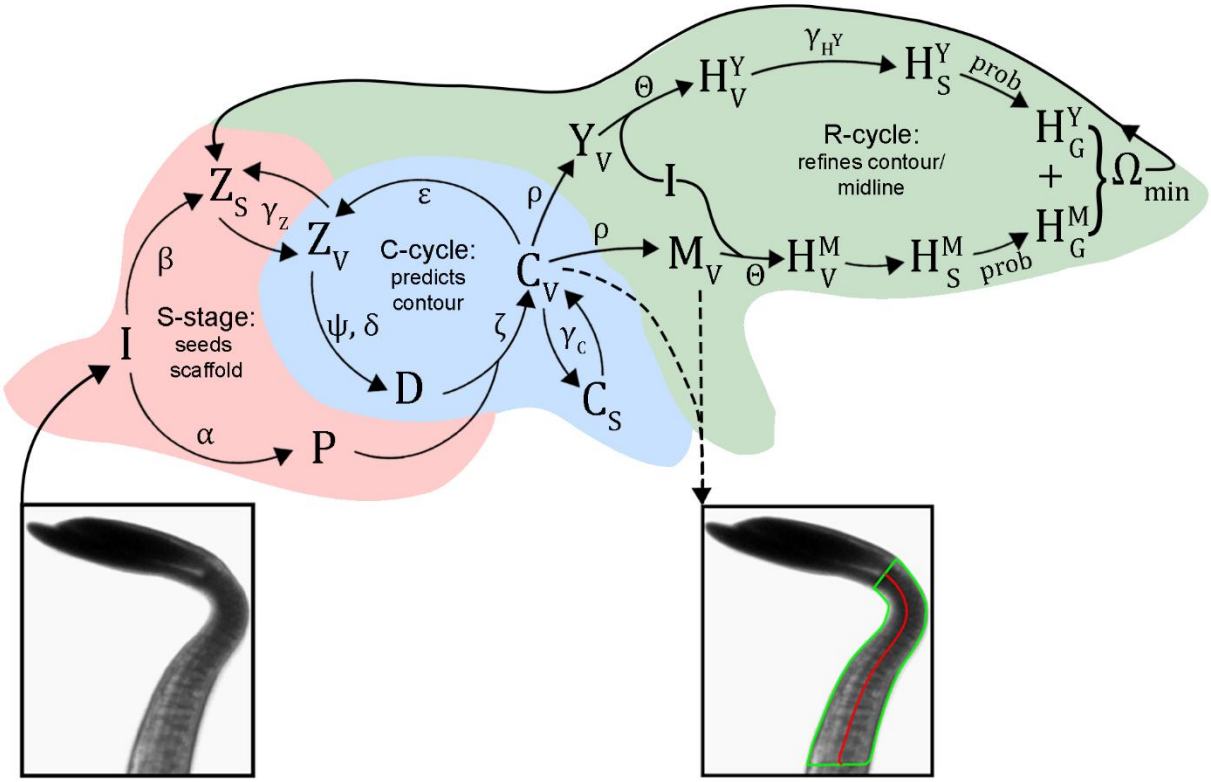

Figure 4. A schematic summary of the software pipeline that produces a hypocotyl-specific midline. Machine learning algorithms trained on ground truth data and other image analysis methods operate in a recursive, generative fashion to produce a midline of the upper hypocotyl that terminates appropriately at the cotyledonary node. The main text explains the functions and the data structures within the S-phase, C-cycle, and R-cycle that together generate the contour-based midline shown as the output.

S-phase

The seeding phase (S-phase) of the algorithm consists of the Find Base and Initialize Scaffold functions. This phase runs an image I through a convolution neural net and predicts the scaffold structure Z_S that is used for the contour generation cycle (C-cycle).

Find Base (α) | $\alpha: I \rightarrow P$

Find Base uses a convolutional neural network to find the hypocotyl base point P of the upper hypocotyl image I (LeCun et al., 2015).

Initialize Scaffold (β) | $\beta: I \rightarrow Z_S$

Initialize Scaffold estimates the curve-like structure Z_S, which provides the context and a buttress for operations that determine the desired contour. This is the representation signature for Z:

$$R_Z \triangleq [\{150,6\},900,10,\gamma_Z,99]$$

C-cycle

The C-cycle is a recursive generative loop that produces and iteratively smooths contours. The main components are a scaffold Z, contour C, and the vector field structure D that connects them. Z consists of a base curve (B) and a reference frame (F) attached to each point on the curve. Therefore, $Z = [\mathrm{B}, \mathrm{F}]$. The displacement vector (D) is attached to each point on Z and is expressed in the frame (F) on the curve. The contour C is generated by adding (D) to the base curve $(C = D + B)$. This C is used to determine a new Z and then a new D which will produce a new C. The process repeats recursively for 15 iterations, where each subsequent iteration yields a smoother C. Functions ψ, δ, ζ, and ε perform this generative and iterative improvement of C. The contour has separate representations for *x* and *y*:

$$R_{CX} \triangleq [\{150,1\},150,7,\gamma_{CX},99] \text{ and } R_{CY} \triangleq [\{150,1\},150,8,\gamma_{CY},99]$$

The predicted displacement vector D produces a contour that needs to be smoothed in a way that respects the ground truth data. Both operations require a vector space constructed from the ground control curves: a vector set spanning the contour curve segments and a vector set

spanning the whole of the closed contour. Both operations project the vector into F at U and then project it out of F at U and is symbolized as ($x = E_w \cdot E_w^{-1} \cdot \tilde{x}$).

Extract Local Information (ψ) | $\psi: \mathrm{I} \times \mathrm{Z_V} \times \mathrm{X^n} \rightarrow \mathrm{V}$

The ψ function uses the Z_V scaffold to extract local image information, which is used to predict the displacement vector D. Z_V is a bundle of a frame and a base curve and serves to relate the many frames along the curve to the frame at the origin of the image. X consists of n rectangular domains, hence X^n in the above statement, along and across the reference frame F, which are sampled and then dimensionally reduced by principal components analysis. The results obtained at each point in Z_V are stored in vector V. Using the bundle's sampling notation from above, ψ produces a vector of local image information $V = I(\mathrm{Z}_V * X^n)$ that the next stage uses. The sampled domains have the representation:

$$R_{X^n} = [\{\{30,30\},\{30,30\},\{100,3\},\{100,3\}\},2400,30,\gamma_n,97]$$

Predict Displacement (δ) | $\delta: V \rightarrow D$

Function δ uses a feedforward network and the pixel information in V to predict a displacement vector D that will produce a C that better approximates the final contour (Sadler et al., 2022). The use of the scaffold curve Z_V in the extraction function ψ allows for a simpler prediction function for a translation and rotation invariant prediction function δ. In other words, the same regression network can be used for the entire hypocotyl.

Generate New Curve (ζ) | $\zeta: Z \times D \rightarrow C$

The ζ function generates a new contour C by first transforming the displacement vector field (D) from F to the image frame and then adding displacement values to the base curve Q. Thus, $C = Q + Z \cdot D$.

Generate Core (ε) | $\varepsilon: w \times C \rightarrow Z_V$

ε takes a range in $\mathbb{I}^1$ of size w to demark a segment of C. A line joining the endpoints of the segment has a midpoint b. At each point b, a unit vector (T) that is along the line joining the segment endpoints and another that is normal to it (N) define a frame F at b (Figure 3B). The window w shifts by one in $\mathbb{I}^1$ to define a new segment with a new midpoint b, and new T and N vectors. The process continues along $\mathbb{I}^1$ to build up a curve B consisting of each point b and a vector F containing the $[T, N]$ reference frames at each point (Figure 3C). Together, B and F form the scaffold curve Z_V (yellow circles in Figure 3C).

The sequence of functions ψ, δ, ζ, and ε is repeated for 15 recursive iterations, as this was sufficient for predictions on the training dataset to approach ground truth results.

R-cycle

After generating a recursively smoothed contour C_V, the refinement cycle (R-cycle) first generates a midline (M_V), and then grades the quality of C_V and M_V described in detail below. The overall grade is the sum of both individual grades. Depending on whether this grade meets a threshold value, the R-cycle will either output the finalized C_V and M_V or adjust the initial scaffold Z_S to make another run through the C-cycle. This cycle is repeated until the threshold is met or a set maximum number of iterations is reached.

The midline M_V is generated using the *Trace Midline* routine described below. The operations that make up the R-cycle use information in the image I to grade the hypocotyl boundary C_V, which is then used to refine the contour's shape and termination of the corresponding midline. A contour's grade is constructed by summing the grades of two products which are derived from C_V and the locally invariant image information from the

midline (H_M) and cotyledon (H_Y). These geometries are relative to the contour, were selected to be anatomically relevant anchors and indicative of the quality of the contour. Figure 3A shows the two elliptical domains located at the cotyledonary node that provide the information in H_Y. A contour C_V is considered highly likely if the image information at those locations is considered probable. The three major steps, ρ, Θ^M, and Θ^Y construct the midline and cotyledon, sample the locally invariant information for these objects and grade the extracted information.

Trace Midline (ρ) | $\rho: C_V \rightarrow [M_V, Y_V]$

This function operates on the contour and produces the geometry for two anchors: the midline and the cotyledon points. The midline curve is produced with a method similar to the one Miller et al. (2007) described. The curve's tangent and normal vectors define a frame (F) which is complexed with the curve to create the midline bundle (M). The other derived product of the contour is the location of the cotyledons. These locations are a fixed distance along the tangent vectors of the top-left and top-right sides of the contour. These positions along with the sampled midline are used to grade the contour's quality.

Extract Local Information (Θ) | $\Theta: I \times A_V \times X \rightarrow H_v^A$

Function Θ is used to create the vectorized representation of the local image information associated with the midline and cotyledon objects H_v^M and H_v^Y. Using the notation for sampling the local image information along the bundle, $H_v^M = \mathrm{I}(M_v \cdot \mathrm{x})$ and $H_v^Y = \mathrm{I}(Y_v \cdot \mathrm{x})$. The samples along the midline and cotyledon have the following signatures:

$$R_M \triangleq [\{50,40\},2000,3,\gamma_M,66] \text{ , } R_Y \triangleq [\{30,30\},900,3,\gamma_Y,45]$$

Any variation of H_v^M and H_v^Y from the expected character of these patches is used to

adjust C, which adjusts the next round of H_v^M and H_v^Y sampling. To estimate any difference from the expected patches, the R-cycle uses two spaces $[\Upsilon, \zeta]$ outfitted with probability distributions $[P_\Upsilon, P_\zeta]$. A vectorized representation of $\mathrm{m} \in H_v^M$ is drawn from the space Υ with probability $P_\Upsilon(\mathrm{m}|\mathrm{C})$, which we represent simply as H_G^M. Similarly, the vectorized representation of the cotyledonary patch is $(\mathrm{y} \in \mathrm{Y}, \zeta, P_\zeta(\mathrm{y}|\mathrm{C}))$, or H_G^Y. The likelihood $L(C)$ of the contour C is then computed as $H_G^M + H_G^Y$. This likelihood is associated with the initial Z_S guess that produced C. The value of Z_S that is fed into the P-cycle is adjusted until the most likely contour is found, determined by the minimization function Ω_{min} in Figure 4 (Nelder and Mead, 1965; Kingma and Ba, 2014).

In summary, three high level constructs are used to trace out the contour: a method to obtain an initial seed (S-phase), generate a contour from this seed (C-cycle), and then grade the generated contour (R-cycle), which can then seed (S-phase) the generative method (C-cycle) with a more probable input. This implementation uses a triple complex $[\mathrm{Z}, \mathrm{D}, \mathrm{C}]$ to predict the contour from local image information and a likelihood function of an action (midline tracing) on the contour to grade the contour.

Constructing and optimizing machine learning models

Three functions in the segmentation pipeline (Figure 4) implement trained learning models to perform their operations. They are α and β from the S-phase and δ from the C-cycle. The ground truth dataset consists of a set of contours (C) traced from upper hypocotyl grayscale images (I) that terminate properly at the cotyledonary node [N = 550]. To reduce variability within the indexing of C, we split the 150 coordinate points in C into left, top, right, and bottom sections such that they contained 60, 15, 60, and 15 points respectively. This normalization

allows the learning models to generate more predictable curves while also placing greater emphasis on the more complex curvilinear left and right regions. These data were then split 80-10-10% into training-testing-validation sets. All models were trained from this same set of ground truth data, although each utilized different elements of the decomposed contour as their inputs to predict different outputs.

Convolutional Neural Net α

Function α in the S-phase (Figure 4) implements a convolutional neural network (CNN) trained on the most basal [20 x 201] pixels of upper hypocotyl images to predict the x-coordinate element of their corresponding base point P ([1 x 2] vector). The CNN consists of three layers that each contain a 2D Convolution, Batch Normalization, and a rectified linear unit. A 2D max-pooling operation then predicts the initialization vector. The layers are fully connected, and a regression layer is used to produce Z_S (MathWorks, 2022).

Convolutional Neural Net β

Function β in the S-phase implements a CNN of similar structure but is trained on the entire upper hypocotyl image ([201 x 201] pixels) to predict the initial scaffold Z_S ([10 x 1] vector). A separate CNN model was made for each of the 10 dimensions within Z_S. We used Bayesian hyperparameter optimization to find the best values for convolution filter size, total filters per layer, dropout percentage layer, and the initial learning rate for each of these models, such that each CNN was uniquely trained and optimized on each dimension in Z_S.

Feedforward Network δ

Lastly, function δ from the C-cycle implements a 5-layer feedforward network with scaled conjugate gradient backpropagation. It was trained on the vectorized local image information V

to predict displacement vectors $\mathbb{D}$.

Measuring segmentation performance

Matthew's Correlation Coefficient (MCC) was used to assess how well our segmentation pipeline performed on ground truth data (Chicco and Jurman, 2020). MCC is generally used to measure association of binary variables, therefore a binary mask was created from the image coordinates of the contours, where contour coordinates are labelled as ones with a small dilation in a 201 x 201 mask of zeros. Comparing identical contours would produce the maximum MCC score of 1. This measurement was selected because it yields a measurement that does not require pairing between two contours, such as those used in Euclidean distance measurements.

The segmentation pipeline processed the training set data [N = 550] and computed the MCC to

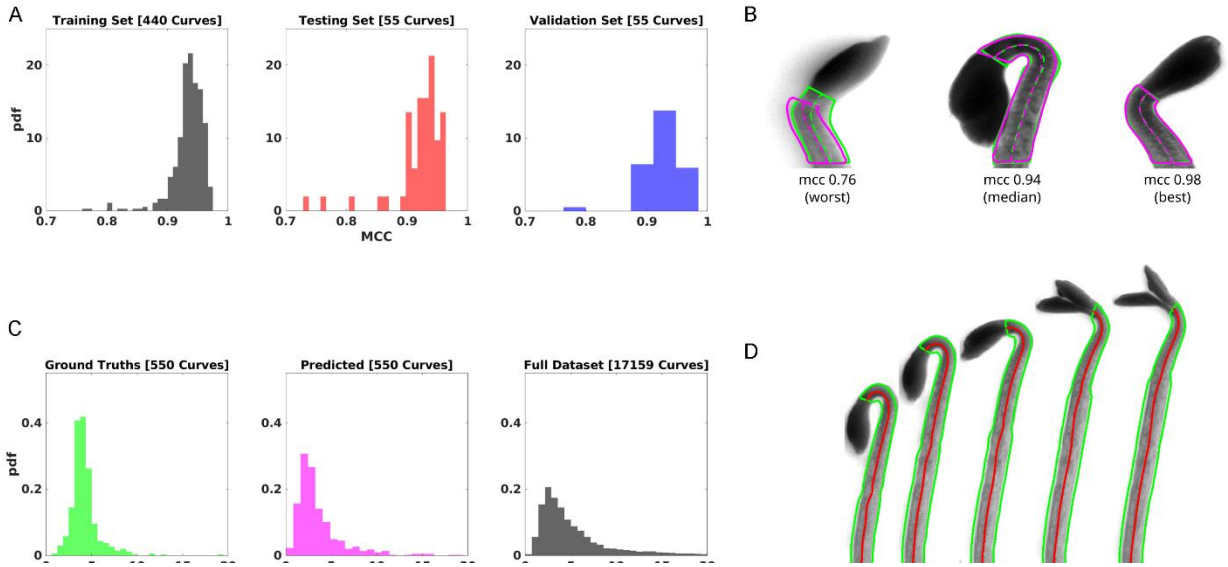

Figure 5. Measuring segmentation performance on ground truth and untraced contours. A) Matthews Correlation coefficients for the training, testing and validation sets. B) Examples of contours and midlines for hypocotyls with poor, median, or high MCC scores. C) Probability grading scores for the ground truths, predicted, and full data sets were similar, indicating the pipeline imitated the human expert. D) An example of a times series of hypocotyls that were successfully processed by HypoQuantyl.

compare the masks of the predicted contour points with their ground truth points. The MCC distribution for our validation set showed a mean of 0.90 ± 0.12 [N = 55]. The mean MCC for the training and testing sets were 0.92 ± 0.08 [N = 440] and 0.91 ± 0.09 [N = 55], respectively. These were all satisfyingly close to a perfect score of 1. To assess performance on untraced hypocotyl images, we processed 61 time course trials with the segmentation pipeline. Each trial contained 1-5 seedlings ($\mu = 4.0$) imaged for 8 hours at 5-minute intervals. Processing these images yielded a total of 23,303 individually segmented curves. We used the probability grading function (Θ) described in the R-Cycle of this pipeline to measure the quality of the outputted C and M_V. The mean of the grades for the top 90% [N = 20,973 curves] of predictions was 7.9 ± 7.3 (Figure 5B). The mean grades from the ground truth set and predictions on the ground truth set were 4.0 ± 4.4 and 4.4 ± 8.1 [N = 550], respectively. The similarity of these scores indicates that HypoQuantyl mimicked the human expert.

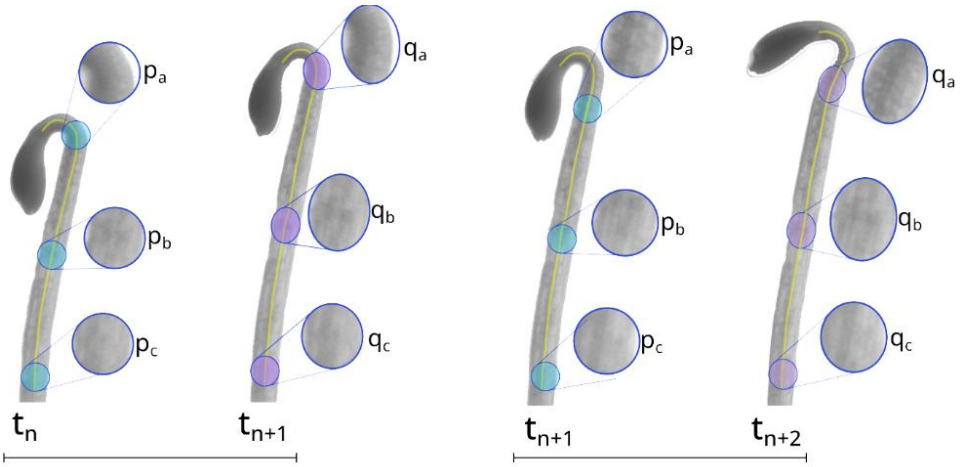

Figure 6. Tracking image patches between two successive frames to measure REGR. Patch p_x in frame *n* is found as q_x in frame *n*+1. Tracking material movement between frames *n*+1 and *n*+2 is based on a new patch p_x being found as q_x. Many patches are tracked between two successive frames but the same patch is not tracked throughout the time series.

Tracking pipeline

The expansion of the cells along the midline causes a mixture of movement in the stem, including elongation, twisting, bending, and swinging. Separating out the internal movement along the midline of the hypocotyl from the swinging and bending motion required the extraction of the midline (Figure 4). Given a midline, the tracking becomes a two-dimensional optimization problem with constraints to prevent collisions between points (Lucas and Kanade, 1981; Meinhardt-Llopis et al., 2013; Philipp et al., 2015). Generally, the second-order solution has five degrees of motion: two translations, two stretches, and one rotation. The isolation of a midline reduces the degrees of freedom to a one-dimensional search along the midline and one stretch value along the midline. The angle of rotation is fixed by the angle given by the midline, stretching along the width of the midline was removed, and two degrees of freedom in the (x,y) image system are reduced to searching through a window of percentages along the midline. A 12-pixel radius disk is used with 60 points along the radius and 96 frames along the angular direction. HypoQuantyl adapted the recently published Patch Track method (Henry et al., 2023) for tracking hypocotyl patches. The only modifications were in the levels of constraints imposed on the amount of translation and stretch permitted. Processing the tracking results into measurements of local material strain rate, the relative elemental growth rate (REGR), was performed as described in Henry et al. (2023) and by Silk and Erickson (Silk and Erickson, 1979; Erickson and Silk, 1980; Silk, 1984).

Figure 7 demonstrates that the entire HypoQuantyl pipeline successfully measured relative elemental growth rate, which is the local rate of material expansion, theoretically the instantaneous strain rate. Figure 7A shows the REGR values determined by HypoQuantyl

mapped on to images of the measured wild-type seedling at selected time points during growth in complete darkness. The greatest local rates of expansion (4-6% h^{-1}) occurred in a zone approximately 1 mm long centered approximately 1 mm from the top of the hypocotyl. The selected images representing this individual seedling show the growth zone to be relatively constant across time and space. Figure 7B shows selected time points of a single seedling growing in darkness before illumination with blue light begins at 2 h. REGR throughout the growth zone is quickly suppressed. Opening of the apical hook quickly follows hypocotyl inhibition. Apical hook opening results from differential growth across the organ, which HypoQuantyl was not designed to measure, but the transient period of high REGR at the apex may reflect the acceleration of expansion on the concave side of the hook that produces the opening. These results indicate that HypoQuantyl can perform the measurements it was designed to make.

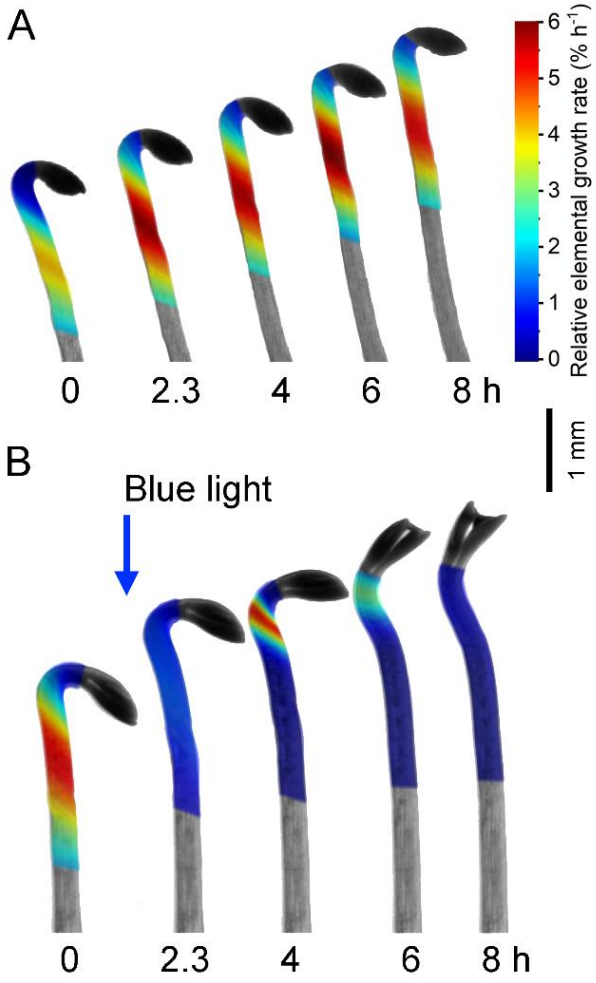

Figure 7. Kinematic analysis of Arabidopsis hypocotyl elongation. A) Relative elemental growth rate (REGR,) measured on a single seedling growing in continuous darkness. B) as in A except this seedling received blue light at the 2 h point. Peak rates of near 6 % h^{-1} reduced quickly to near 0.

Using HypoQuantyl to analyze hypocotyl growth in photoreceptor mutants

In one set of experiments, wild-type seedlings were maintained in total darkness as images

were collected every 5 min. Figure 8A shows the average spatiotemporal distribution (map) of REGR for wild-type seedlings in darkness. The REGR map shows that the major expansion occurred in a zone extending from 0.3 to 1.5 mm from the top of the hypocotyl. REGR values reached 4% h^{-1} in this region. They were not constant. During 7 h of growth in darkness, the average REGR response map displayed four peaks and three troughs in the temporal direction. The peaks were spaced between 1.5 and 2.5 h apart. Along the axial direction, the single REGR peak migrated basally from approximately 0.7 to 1.3 mm from the apex during the recording period. In another set of experiments, continuous illumination with red light began after 2 h of growth in the dark. Over the ensuing 5 h, REGR decreased throughout the 0.7-1.3 mm elongation zone (Figure 8B). This slowly developing inhibition of hypocotyl elongation is a phytochrome-mediated response. Genetic evidence indicates that PhyB is the photoreceptor that contributes most to the response because *phyB* mutants have a long hypocotyl when grown in red light (Somers et al., 1991).

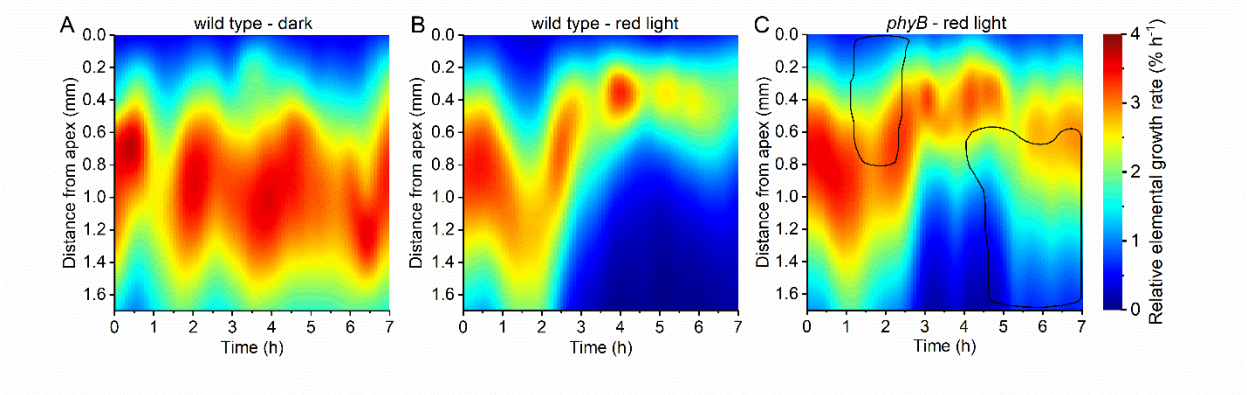

Figure 8. REGR maps depicting the effects of red light on hypocotyl elongation. A) Wild-type seedlings grown in continuous dark, average of 10 individual seedling maps. B) Wild-type seedlings grown in darkness for 2 h before continuous irradiation with red light average of n = 10. C) *phyB* mutant seedlings grown in darkness for 2 h before continuous irradiation with red light average of n = 7. The black contour lines surround areas are that significantly different than the wild-type response, p=0.05.

Consistent with the long-hypocotyl endpoint phenotype of *phyB* mutants, REGR remained high across much of the regular elongation zone. The black contour line indicates where in space and time this average *phyB* result differed from the wild-type average response according to t-tests of statistical significance. The significantly different region from 4.5 h to 7 h confirmed the timing of PHYB action Parks et al. (1999) reported based on hypocotyl lengths measured over time. What the previous study could not address was where along the hypocotyl PHYB acted. Figure 8B shows that growth was significantly greater (inhibition significantly reduced) in *phyB* everywhere below 0.6 mm after 4.5 h. An earlier period of significant difference in the REGR map is probably the kinematic basis of a rapid, transient period of growth inhibition that Parks et al. (1999) determined to be caused by a combination of PHYA and PHYB action. Figure 8B shows that this initial, transient phase of inhibition occurred in a region of the hypocotyl above the later-inhibited zone. Thus, growth inhibition mediated by the PHYB photoreceptor occurs first and transiently in the apical-most 0.8 mm of the hypocotyl, and later in the region below 0.8 mm.

Blue light inhibits hypocotyl elongation more rapidly than red light, beginning even within a few seconds (Spalding and Cosgrove, 1989; Parks et al., 1998). Figure 9A shows that the growth zone in darkness, from approximately 0.3 mm to 1.5 mm, collapses quickly after the onset of blue light. This figure shows the kinematic basis of the well-studied rapid inhibition of hypocotyl growth by blue light that pea, cucumber, *Sinapis*, and Arabidopsis seedlings display (Cosgrove, 1981; Cosgrove, 1982; Spalding and Cosgrove, 1989). A previous study showed that

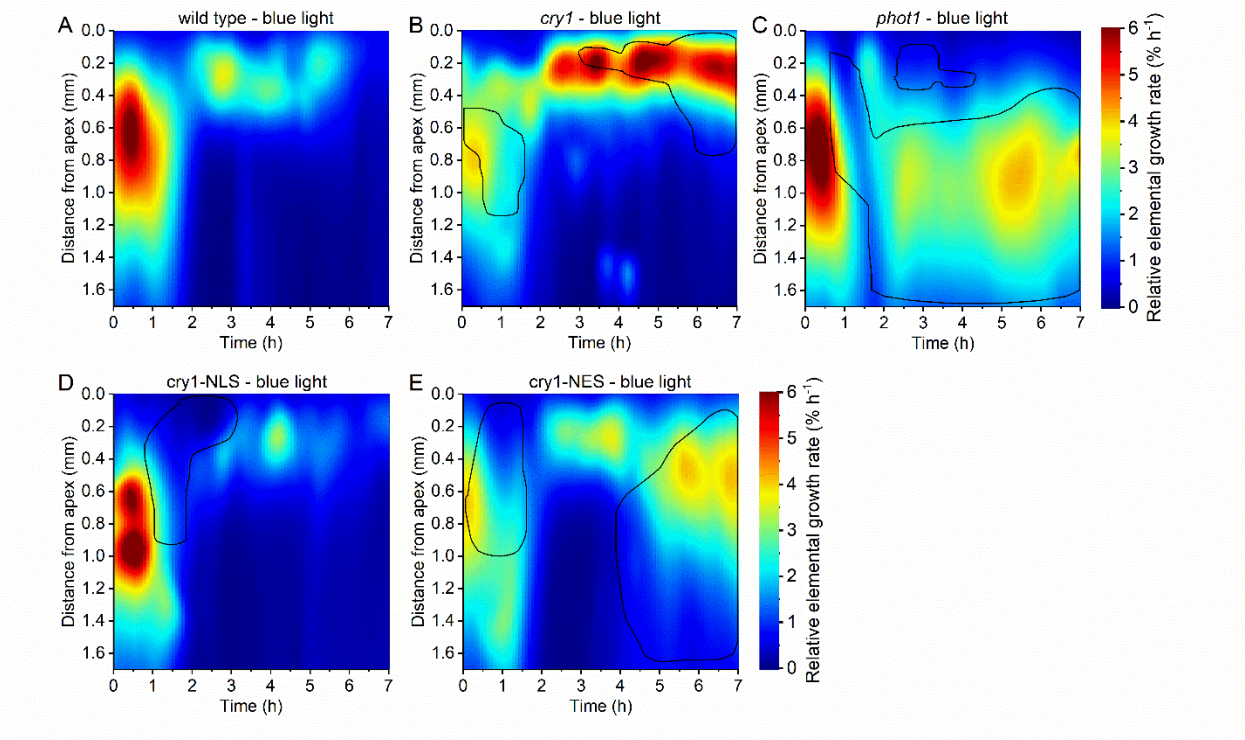

Figure 9. REGR maps depicting the effects of blue light on hypocotyl elongation. A) Wild type, average of n = 1 B) *cry1* mutant, n = 14 C) *phot1* mutant, n = 10 D) *cry1* transformed with CRY1 translationally fused to a nuclear localization signal, n = 8 E) *cry1* transformed with CRY1 translationally fused to a nuclear export signal, n = 10.
The black contour lines surround areas are that significantly different than the wild-type response, p=0.05.

the initial period of inhibition was due to the action of the PHOT1 blue light receptor (Folta et al., 2001). The kinematic results in Figure 9B show that REGR in a *phot1* mutant remains higher than wild type (is less inhibited) across much of the regular elongation zone beginning immediately and persisting through the recording period. Statistical analysis detected an additional, small region of difference from the wild type between 0.1 mm and 0.3 mm and lasting for 2 h after the onset of blue light. The exact timing of changes is difficult to define in these kinematic data because the patterns are changing in the dark before the treatment begins. This small transient is worth noting because it indicates that the mutant is more inhibited than the wild type in this restricted, very apical region. Because the *phot1* mutant

does not display a long-hypocotyl endpoint phenotype, its inhibitory action must not persist. CRY1 causes persistent inhibition. The initial phase of inhibition occurs normally in *cry1* mutants, presumably because PHOT1 is mediating that first phase, but after 30 min of blue light, elongation rate increases in *cry1*. These results were interpreted to mean that the initial phase of inhibition controlled by PHOT1 must be replaced by a CRY1-dependent mechanism and the two must be coordinated well in time in a wild-type seedling. It was proposed that the CRY1 mechanism must strengthen as the PHOT1 mechanism weakens. The kinematic results in Figure 9B,C support a new mechanism based on unprecedented kinematic data. In *cry1*, the main elongation zone remains inhibited during the recording period. The apparent escape from inhibition is not due to a resumption of growth in the main elongation zone (0.3-1.5 mm from the top), but to a new region of very high REGR with peak local expansion occurring only 0.2 mm from the top of the hypocotyl. A region of the hypocotyl that was previously not contributing to elongation becomes the source of elongation. The role of CRY1 in a wild-type seedling receiving blue light is to prevent these cells at the apical end of the hypocotyl from elongating.

CRY1 is in the cytoplasm and nucleus of cells. Wu and Spalding (2007) manipulated its subcellular localization by expressing CRY1 fused to a nuclear localization signal (NLS) in a *cry1* mutant. Wu and Spalding (2007) also fused a nuclear export signal (NES) to CRY1 and expressed it in a *cry1* mutant. Measurements of hypocotyl elongation by the HYPOTrace method (Wang et al., 2009) showed that the nuclear localized version of CRY1 completely rescued the *cry1* growth response while the cytoplasmic version had no effect on the mutant phenotype. Kinematic analysis of these same lines produced the results in Figure 9D, E. The CRY1-NES

produced a REGR map that was essentially like the unaltered mutant, sharing the same regions of statistical difference while the CRY1-NLS response was like the wild type. This molecular rescue experiment validates the conclusion that, in blue light, CRY1 prevents cell elongation in the most apical part of the hypocotyl. In the absence of CRY1, those cells elongate. The kinematic analysis indicates that CRY1 does not inhibit the primary region that was expanding before the light treatment but prevents cells above that zone from contributing to the lengthening process in the presence of blue light.

Discussion

HypoQuantyl is an end-to-end analysis pipeline for characterizing the kinematic basis of hypocotyl growth over time scales relevant to studies of photomorphogenesis. The most novel aspect of the pipeline is its method for discovering a faithful midline specific to the hypocotyl. This part of the HypoQuantyl solution can be described as a recursive engine with an internal structure that generates, grades, and optimizes the discovery of a curve in a digital image. A curve that bounds a structure is a contour, and contour isolation is a prominent topic in computer vision and biological imaging (Blake et al., 1988; Kass et al., 1988; Xi et al., 2017; Rabeh, et al., 2017). At a high level, the part of HypoQuantyl summarized in Figure 4 is a machine learning-based algorithm that collapses a closed contour down on to a specific target. It was developed and trained to isolate hypocotyls from grayscale images, but the architecture of the S-phase, C-cycle, and R-cycle could be more generally applicable in plant biology research, where methods for defining shapes, particularly through image analysis, and then treating them as mathematical objects has been recognized as a critical need (Bucksch et al., 2017). Measuring the effects of mutations (phenotypes) with the objectivity, precision, and

throughput such methods can deliver creates data that advances our understanding of the genotype-phenotype relationship. Ideally, every aspect of plant growth and development could be measured using the methods HypoQuantyl brings to bear on the Arabidopsis hypocotyl growing and responding to light.

The ability of HypoQuantyl to faithfully segment thousands of hypocotyls in various stages of de-etiolation, and map the distribution of material expansion within them, generated an unprecedented description of how fast, where, and when stem material expanded. The results obtained with dark-grown seedlings (Figure 8A) closely matched the results reported by Bastien et al. (2016) with their KymoRod software. They also found REGR of 3-4% h^{-1} in an apical growth zone approximately 2 mm long. Thus, the tracking and kinematic analyses within HypoQuantyl appear to function as well as those in KymoRod. Where HypoQuantyl primarily distinguishes itself from KymoRod is in the automation of hypocotyl segmentation (Figure 3) that the machine learning approach enabled. HypoQuantyl operates without human inputs. In fact, the computations were performed on a distributed high-throughput computing resource at the University of Wisconsin Center for High Throughput Computing managed by HTCondor job scheduling software (Thain et al., 2005).

The usefulness of HypoQuantyl was demonstrated here in a study of light-induced inhibition of hypocotyl elongation. The kinematic results can be interpreted in the context of much previous research into the molecular and physiological mechanism of the growth inhibition. Light in the blue region of the spectrum inhibits hypocotyl elongation very rapidly. The inhibition is due to a change in the rheological properties of the cell wall. Specifically, blue light reduces the loosening rate of bonds between polymers in the cell wall that are bearing the

stress imposed by cellular turgor pressure (Cosgrove, 1988). A 'tightening' of the cell wall quickly follows the onset of blue light to explain the growth inhibition. Some evidence indicates that the effect on wall loosening is due to inhibition of the H^+-ATPase at the plasma membrane, which would be expected to raise the pH of the wall, which would inhibit the activity of the expansin proteins. Because PHOT1 is known to control the activity of the H^+-ATPase at the plasma membrane of stomatal guard cells, albeit in the activating direction (Yamauchi et al., 2016), and because PHOT1 resides at the plasma membrane in hypocotyl cells (Sakamoto and Briggs, 2002), we suggest that PHOT1 inhibits the H^+-ATPase in the main elongation zone to inhibit expansion. Thus, we propose that the initial inhibition of elongation known to be PHOT1-mediated occurs in the main elongation zone, possibly due to inhibition of the plasma membrane H^+-ATPase in these expanding cells. The surge in growth observed after 30 min in *cry1* mutants is not, as previously thought, due to a dissipation of this initial inhibition. The REGR maps (Figure 7) indicate that the main elongation zone where PHOT1 began the response remains inhibited. The rapid expansion in *cry1* mutants after 30 min is due to cells above the main elongation zone becoming competent to expand. Somehow, when CRY1 is activated by blue light, it makes cells in the apical-most 0.2 mm of the hypocotyl unable to expand. This state change does not occur in the *cry1* mutant. Essentially, a new elongation zone is established, limited on the apical end by the cotyledonary node and on the basal end by PHOT1-inhibited cells. Perhaps CRY1 control over this region of the hypocotyl serves to maintain a reserve of extension capability should the seedling, in a natural scenario, become covered again by soil or leaf litter. Over time in darkness, CRY1 reverts biochemically to its dark state, which may relieve the block of material in this region of the hypocotyl and allow

expansion in a re-darkening situation.

Molecular genetic studies of CRY1 provide some possible mechanisms to explain how CRY1 may lock cells into a non-expanding state. Previous work from our lab showed that CRY1 must be in the nucleus to maintain this apical region in a non-responsive state (Wu and Spalding, 2007). In the nucleus, the light-sensing domain of CRY1 interacts with AUX/IAA proteins (Xu et al., 2018), which must be degraded for this growth hormone to promote cell expansion. The CRY1-AUX/IAA interaction is thought to stabilize the AUX/IAA, prevent its degradation, and thereby inhibit auxin responses. Remarkably, PHYB interacts with the same AUX/IAA proteins (Xu et al., 2018). This raises the possibility that the CRY1-mediated inhibition of expansion in a short apical region of the hypocotyl and PHYB-mediated inhibition of the standard growth zone are both due to suppression of auxin responses. This is consistent with the observation that auxin transport through the hypocotyl mediated by the ABCB19 protein contributes to the extra phase of elongation that *cry1* mutants display in blue light, and *phyB* mutants display in red light (Wu et al., 2010).

None of the molecular genetic investigations of cryptochrome actions that Wang and Lin (2020) recently reviewed focused on a specific location or cell type. In fact, these authors highlighted the fact that location of action is understudied.

"… plant cryptochromes appear to express ubiquitously, but light is unlikely to have the same effects on different cells and organs of a plant. *Therefore, how to distinguish the specific functions of cryptochromes in the specific photoresponses of individual cells is another challenge.* Recent advances in single-cell RNA and protein analysis technologies would likely bring new insights about the novel and cell-specific functions of plant cryptochromes."

The emphasis is mine.

The HypoQuantyl analysis of the *cry1*, *phot1*, and *phyB* mutants provides exactly the spatiotemporal information called for in this quote.

Materials and Methods

Seedling culture

Seeds of *Arabidopsis thaliana* were sown, stratified, and cultivated on vertical agar plates as described in Wang et al. (2007). Seedlings were used after 3 d of growth in total darkness.

Image acquisition

A clear plastic Petri plate with seedlings growing vertically on the surface of agar was mounted perpendicular to the optical axis of a macro video zoom lens (18-108 mm *f*/2.5, www.edmundoptics.com) fitted to a charge-coupled device camera (Marlin F-146B; www.alliedvision.com) that was controlled by a computer. A close-up +4 lens (www.tiffen.com) attached to the zoom lens increased magnification. An infrared-pass filter (R72, www.hoyafilterusa.com) permitted 948-nm infrared radiation emitted by a BL020201 backlight (www.advancedillumination.com) placed behind the seedlings to reach the camera, which was made sensitive to infrared by removal of the internal infrared-blocking filter. This platform produced images of growing seedlings at a resolution of 184 px mm^{-1}, even in the complete absence of visible light. This arrangement ensured that blue light produced by a LED source described in Wang et al. (2007) treated the seedlings with a fluence rate of approximately 80 µmol m^{-2} s^{-1} without affecting the image the camera collected. The LED red light source described in Parks et al. (1999) produced a fluence rate of approximately 100 µmol m^{-2} s^{-1}. All experiments were performed in a photobiology darkroom. Some manipulations required brief use of a dim green safelight.

The camera collected images every 5 min. The indicated light treatment began at frame

24, 2 h after the start of recording in complete darkness. Image collection continued every 5 min for 6 h. The 96 images per trial were stored in tagged image file (.TIF) format. These time series of images were used to develop the HypoQuantyl analysis pipeline, and they were the raw experimental data used to characterize the kinematics of light responses in the wild type and the indicated mutant genotypes.

References

Ahmad M, Cashmore A (1993) *HY4* gene of *A. thaliana* encodes a protein with characteristics of a blue-light photoreceptor. Nature **366**, 162–166. https://doi.org/10.1038/366162a0

Aris, R. (1962). Vectors, Tensors and the Basic Equations of Fluid Mechanics. Dover, New York NY pp 320

Arsovski AA, Galstyan A, Guseman JM, Nemhauser JL. (2012) Photomorphogenesis. The Arabidopsis Book **10**, e0147 https//doi.org/10.1199/tab.0147

Bastien R, Legland D, Martin M, Fregosi L, Peaucelle A, Douady S, Moulia B, Höfte H. (2016) KymoRod: a method for automated kinematic analysis of rod-shaped plant organs. Plant J. **88**, 468-475

Ben Rabeh A, Benzarti F, & Amiri H (2017) Segmentation of brain MRI using active contour model. International Journal of Imaging Systems and Technology **27**, 3-11 https://doi.org/10.1002/ima.22205

Blake A, Isard M (1998) Active Contours. Springer London. https://doi.org/10.1007/978-1-4471-1555-7

Bucksch A et al. Morphological plant modeling: unleashing geometric and topological potential within the plant sciences (2017) Frontiers in Plant Sciences **8**, 900. https://doi.org/ 10.3389/fpls.2017.00900

Cartan É (1925) La géométrie des espaces de Riemann. Mémorial des sciences mathématiques 73 p. http://eudml.org/doc/192543

Chicco D, Jurman G (2020) The advantages of the Matthews correlation coefficient (MCC) over F1 score and accuracy in binary classification evaluation. BMC Genomics **21,** 6. https://doi.org/10.1186/s12864-019-6413-7

Cosgrove DJ (1981) Rapid suppression of growth by blue light: Occurrence, time course, and general characteristics. Plant Physiology **67,** 584-590

Cosgrove DJ (1982) Rapid inhibition of hypocotyl growth by blue light in *Sinapis alba*. Plant Sci. Lett. **25**, 305-312

Cosgrove DJ (1988) Mechanism of rapid suppression of cell expansion in cucumber hypocotyls after blue light irradiation. Planta **176**, 109-116

Dowson-Day MJ, Millar AJ (1999) Circadian dysfunction causes aberrant hypocotyl elongation patterns in Arabidopsis. Plant Journal **17**, 63-71 https://doi.org/10.1046/j.1365-313X.1999.00353.x

Ehresmann C. Les connexions infinitésimales dans un espace fibré différentiable. Colloque de Topologie (Espaces fibrés), Bruxelles, 1950. Paris: Georges Thone, Liège; Masson et Cie.

pp. 29–55

Erickson RO, Silk WK (1980) The kinematics of plant growth. Scientific American **242**, 134,151

Folta KM, Spalding EP (2001) Unexpected roles for cryptochrome 2 and phototropin revealed by high-resolution analysis of blue-light-mediated hypocotyl growth inhibition. Plant Journal **26**, 471-478

Hall, H and Ellis, B (2012) Developmentally equivalent tissue sampling based on growth kinematic profiling of Arabidopsis inflorescence stems. New Phytologist **194**, 287–296

Henry AR, Miller ND, Spalding EP. (2023) Patch Track software for measuring kinematic phenotypes of Arabidopsis roots demonstrated on auxin transport mutants. International Journal of Molecular Sciences **24**: 16475 https://doi.org/10.3390/ijms242216475

Kass M, Witkin A, Terzopoulos D (1988). Snakes: Active contour models. International Journal of Computer Vision **1**, 321-331 https://doi.org/10.1007/bf00133570

Kingma DP, Ba J (2014) Adam: A Method for Stochastic Optimization (Version 9). arXiv:1412.6980v9

LeCun Y, Bengio Y, Hinton G (2015) Deep learning. Nature **521**, 436-444 https://doi.org/10.1038/nature14539

Lucas BD, Kanade T (1981) An iterative image registration technique with an application to stereo vision. In Proceedings of the 7th International Joint Conference on Artificial Intelligence - Volume 2 (pp. 674–679). Morgan Kaufmann Publishers Inc.

Meijer G (1968) Rapid growth inhibition of gherkin hypocotyls in blue light. Acta Botanica Neerlandica **17**, 9-14

Meinhardt-Llopis E, Sánchez Pérez J, & Kondermann D (2013). Horn-Schunck optical flow with a multi-scale strategy. Image Processing On Line **3**, 151-172 https://doi.org/10.5201/ipol.2013.20

Miller ND, Parks BM, Spalding EP (2007) Computer vision analysis of seedling responses to light and gravity Plant Journal, 52(2), 374?381. https://doi.org/10.1111/j.1365-313x.2007.03237.x

Nelder JA, Mead R (1965) A simplex method for function minimization. The Computer Journal **7**, 308-313 https://doi.org/10.1093/comjnl/7.4.308

Otsu N (1979) A threshold selection method from gray-level histograms. IEEE Transactions on Systems, Man, and Cybernetics **9**, 62-66

Parks BM, Quail PH (1993) *hy8*, a new class of Arabidopsis long hypocotyl mutants deficient in functional phytochrome A. Plant Cell **5**, 39–48 https://doi.org/10.1105/tpc.5.1.39

Parks, BM, Cho, MH, Spalding, E. (1998) Two genetically separable phases of growth inhibition induced by blue light in Arabidopsis seedlings. Plant Physiology, **118**, 609-615.

Parks BM, Spalding EP (1999) Sequential and coordinated action of phytochromes A and B during *Arabidopsis* stem growth revealed by kinetic analysis. Proceedings of the National Academy of Sciences USA **96**: 14142-14146

Pearson, K. (1901). LIII. On lines and planes of closest fit to systems of points in space. The London, Edinburgh, and Dublin Philosophical Magazine and Journal of Science, 2(11), 559-572. https://doi.org/10.1080/14786440109462720

Philipp Fischer, Alexey Dosovitskiy, Eddy Ilg, Philip Häusser, Caner Hazırbaş, Vladimir Golkov, Patrick van der Smagt, Daniel Cremers, Thomas Brox (2015). FlowNet: Learning Optical Flow with Convolutional Networks (Version 2). arXiv. https://doi.org/10.48550/ARXIV.1504.06852

Sadler, I., Reimann, N., & Sambell, K. (2022). Feedforward practices: a systematic review of the literature. Assessme; Evaluation in Higher Education **48**, 305,320 https://doi.org/10.1080/02602938.2022.2073434

Sakamoto K, Briggs WR (2002) Cellular and subcellular localization of phototropin 1. Plant Cell **14**, 1723–1735, https://doi.org/10.1105/tpc.003293

Silk WK, Erickson RO (1979) Kinematics of plant growth. Journal of Theoretical Biology **76**, 481-501

Silk WK (1984) Quantitative descriptions of development. Annual Review of Plant Physiology **35**, 479-518

Somers, D.E., Sharrock, R.A., Tepperman, J.M., and Quail, P.H. (1991) The *hy3* long hypocotyl mutant of Arabidopsis is deficient in phytochrome B. Plant Cell **3**, 1263-1274

Spalding EP, Cosgrove DJ (1989) Large plasma-membrane depolarization precedes rapid blue-light-induced growth inhibition in cucumber. Planta 178: 407-410

Spalding EP, Cosgrove DJ (1993) Influence of electrolytes on growth, phototropism, nutation and surface potential in etiolated cucumber seedlings. Plant Cell & Environment **16,** 445-451

Thain D, Tannenbaum T, Livny M (2005) Distributed computing in practice: the Condor experience. Concurrency and Computation: Practice and Experience **17**, 323-356

The MathWorks Inc. (2022). MATLAB version: 9.13.0 (R2022b), Natick, Massachusetts: The MathWorks Inc. https://www.mathworks.com

Wang L, Uilecan IV, Assadi AH, Kozmik CA, Spalding EP (2009) HYPOTrace: image analysis software for measuring hypocotyl growth and shape demonstrated on Arabidopsis seedlings undergoing photomorphogenesis. Plant Physiology **149**, 1632-1637

Wang Q, Lin C (2020) Mechanisms of cryptochrome-mediated photoresponses in plants Annual Review of Plant Biology **71**, 103-129

Wu G, Spalding EP (2007) Separate functions for nuclear and cytoplasmic cryptochrome 1 during photomorphogenesis of Arabidopsis seedlings. Proceedings of the National Academy of Sciences USA **104**, 18813-18818

Wu G, Cameron JN, Ljung K, Spalding EP (2010) A role for ABCB19-mediated polar auxin transport in seedling photomorphogenesis mediated by cryptochrome 1 and phytochrome B. The Plant Journal **62**, 179-191 https://doi.org/10.1111/j.1365-313X.2010.04137.x

Xu F, He S, Zhang J, Mao Z, Wang W, Li T, ... & Yang HQ (2018) Photoactivated CRY1 and phyB interact directly with AUX/IAA proteins to inhibit auxin signaling in Arabidopsis. Molecular Plant **11**, 523-541

Yamauchi S, Takemiya A, Sakamoto T, Kurata T, Tsutsumi T, Kinoshita T, Shimazaki KI (2016) The plasma membrane H+-ATPase AHA1 plays a major role in stomatal opening in response to blue light. Plant Physiology **171**, 2731-2743

Xi X, Shi H, Han L, Wang T, Ding HY, Zhang G, Tang Y, Yin Y (2017) Breast tumor segmentation with prior knowledge learning. Neurocomputing, **237**, 145-157 https://doi.org/10.1016/j.neucom.2016.09.067